Journal of
Materials Chemistry B

ROYAL SOCIETY
OF CHEMISTRY

PAPER

View Article Online
View Journal | View Issue

Cite this: *J. Mater. Chem. B*, 2023, **11**, 10234

Wool keratin/zeolitic imidazolate framework-8 composite shape memory sponge with synergistic hemostatic performance for rapid hemorrhage control†

Feng Sang,‡[ab] Xiao Yang, ‡[a] Jiahui Hao,[ab] Yuzhen Wang,[b] Xiaoqin Si,[a] Xujian Li,[a] Luqi Pan,[a] Zhaipu Ma*[c] and Changcan Shi *[ab]

Uncontrollable hemorrhage and subsequent wound infection pose severe threats to life, especially in the case of deep, non-compressible, massive bleeding. Here, a wool keratin/zeolitic imidazolate framework-8 (WK/ZIF-8) composite shape memory sponge is prepared by incorporating ZIF-8 nanoparticles into wool keratin. The combination of keratin and ZIF-8 particles not only reduces the effect of ZIF-8 particles on cell viability but also bolsters the mechanical properties of the keratin sponge and endows it with antibacterial efficacy. Due to the synergistic effect of the excellent hemostatic performance of keratin and Zn^{2+} release from ZIF-8 nanoparticles, the porous structure suitable for blood cell adhesion and the shape recovery ability of sponges, the WK/ZIF-8 composite sponge exhibits superior hemostatic performance to commercial medical sponges in SD rat and rabbit hemorrhage models. In addition, *in vitro* and *in vivo* antibacterial experiments demonstrate the anti-infection activity of the composite sponge. Overall, the WK/ZIF-8 composite sponge provides a promising approach to rapidly control bleeding and promote wound healing.

Received 24th July 2023,
Accepted 9th October 2023

DOI: 10.1039/d3tb01660a

rsc.li/materials-b

1. Introduction

In cases of war and life traumas, cardiovascular collapse, failure of tissue oxygenation, ischemia, and organ dysfunction caused by uncontrolled massive hemorrhage are the major causes of death. Most of such fatalities occurred in harsh environments prior to hospital admission or surgical treatment.[1–3] To date, a variety of hemostatic materials have been investigated and developed, including hemostatic bandages, gauze, zeolites, chitosan-based powders, and gelatin-based sponges.[4] However, these hemostatic materials have limitations when applied to uncontrolled massive bleeding wounds on the battlefield or in real life, such as their inability to deliver to the irregularly shaped and non-compressible bleeding site.[3,5] In addition, wounds are susceptible to bacterial infection after prolonged exposure to air.[6] Therefore, it is crucial for researchers to develop a novel multifunctional hemostatic material that can quickly and effectively control massive bleeding, kill bacteria, and accelerate wound healing.

Keratin, a natural protein that is widely found in animal tissues such as wool, skin, nails, and feathers, and readily attainable from human hair, has received considerable attention in the field of hemostasis and wound healing in recent years.[7,8] This can be attributed to its low price, excellent biocompatibility, remarkable hemostatic abilities, improved cell adhesion properties, reduced immune response, and accelerated wound-healing properties.[9,10] It has been reported that keratin can promote hemostasis by significantly shortening the plasma coagulation lag time and increasing lateral fiber assembly and is able to maintain its activity under simulated coagulopathy conditions.[11,12] However, as a hemostatic agent, keratin has limitations when used in the treatment of uncontrolled bleeding wounds. Because the disulfide bonds in wool and hair are cleaved during the extraction of keratin, pure keratin materials generally have low mechanical strength and lack the stability required for hemostatic applications.[13–16] In addition, keratin lacks antimicrobial properties, limiting its efficacy in combating the harsh environment of patients with uncontrolled bleeding prior to hospital admission or surgery. Therefore, in order to broaden the application prospects of keratin as a hemostatic agent, it is necessary to find a way to overcome these deficiencies and further enhance its hemostatic properties.

---

[a] *Wenzhou Institute, University of Chinese Academy of Sciences, Wenzhou, Zhejiang 325011, China. E-mail: shicc@ucas.ac.cn; Tel: +86-577-88017500*

[b] *School of Ophthalmology and Optometry, School of Biomedical Engineering, Wenzhou Medical University, Wenzhou, Zhejiang 325027, China*

[c] *School of Life Sciences, Hebei University, Baoding, Hebei 071000, China. E-mail: wdwsjlxx@163.com*

† Electronic supplementary information (ESI) available. See DOI: https://doi.org/10.1039/d3tb01660a

‡ Feng Sang and Xiao Yang contributed equally to this work.

Zeolitic imidazolate framework-8 (ZIF-8), a form of metal–organic framework (MOF), consists of zinc(II) clusters linked by 2-methylimidazole bridges.[17] Due to its large surface area, good stability, and low cost, it has attracted much attention from researchers.[18,19] ZIF-8 is highly pH-responsive, is stable under physiological conditions and could continuously release zinc ions (Zn^{2+}) in the acidic environment of the wound.[20–22] It has been reported that the released zinc ions can not only kill bacteria by disrupting their fluid membranes but also improve keratinocyte motility and aid in wound healing.[23] More importantly, Zn^{2+} can serve as a cofactor to induce activation of coagulation factors XII to instigate the rest of the coagulation cascade and accelerate the production of thrombin and fibrin, thereby promoting coagulation.[24,25] In addition, as nanofillers can provide structural support to the polymer network and enhance mechanical strength,[26] we speculated that ZIF-8 nanoparticles have the potential to improve the mechanical properties of keratin sponges.

In this study, we designed and developed a keratin-based antibacterial shape memory hemostatic sponge that could rapidly control massive arterial hemorrhage and non-compressible deep bleeding. The thiol groups inherent in keratin were exploited without any additional chemical modification of the keratins, which promoted the biocompatibility of the sponge greatly. The Zn^{2+} released from ZIF-8 acted as a cross-linking agent to form Zn–S bonds with sulfhydryl groups and to cross-link between sulfhydryl groups.

The dynamic exchange reaction between disulfide bonds (S–S) and zinc–thiolates (Zn–S) led to the formation of a network structure between the keratin molecules. The combination of the keratin and ZIF-8 particles not only reduced the effect of the ZIF-8 particles on cell viability and bolstered the mechanical properties of the keratin sponge but also endowed the keratin sponge with antibacterial efficacy and improved its hemostatic ability. The WK/ZIF-8 composite sponge exhibited superior hemostatic performance to commercial medical sponges and pure keratin sponges in the rat liver bleeding model, rat femoral artery model, rat and rabbit liver penetrating injury model, and rabbit ear artery bleeding model. In addition, the composite sponge could also promote wound healing of bacterially infected full-thickness skin wounds. All results indicated that the WK/ZIF-8 composite sponge could rapidly control massive arterial hemorrhage and non-compressible deep bleeding, and aid in wound healing.

2. Materials and methods

2.1 Materials

Wool keratin (WK) powders were purchased from Xian Ding Biotechnology Co., Ltd (Shanghai, China). Sodium sulfide nonahydrate ($Na_2S\cdot9H_2O$), methanol (CH_4O), and 2-methylimidazole (MeIm) were purchased from Shanghai Macklin Biochemical Technology Co., Ltd. Sodium dodecyl sulfate (SDS) was purchased from Aladdin Biochemical Technology Co., Ltd (Shanghai, China). Zinc nitrate hexahydrate was obtained from Chengdu Kelon Chemical Co., Ltd (Sichuan, China). Lactate dehydrogenase (LDH) was purchased from Chengdu Yuannuo Tiancheng Technology Co., Ltd. Phosphate buffer saline (PBS, PH 7.4) was provided by Procell Life Science & Technology Co., Ltd. Sprague–Dawley (SD) rats and New Zealand white rabbits were provided by the Experimental Animal Center, Wenzhou Research Institute, University of Chinese Academy of Sciences (Wenzhou, China). All other reagents mentioned above were of analytical grade and were used as received without further purification.

2.2 Preparation of ZIF-8

ZIF-8 was prepared as follows: 0.3 g of zinc nitrate hexahydrate ($Zn(NO_3)_2\cdot6H_2O$, purity 99%) and 0.66 g of MeIm (purity 99%) were dissolved separately in 14.3 mL of methanol. The prepared zinc nitrate hexahydrate methanolic solution and MeIm methanolic solution were mixed and stirred at room temperature (22 °C) for 2 h. ZIF-8 dispersion was centrifuged at 10 000 rpm for 10 min, and the pellet was collected and washed 3 times with methanol to remove excess zinc nitrate and MeIm. The white ZIF-8 was obtained after drying the prepared ZIF-8 powder at 70 °C for 12 h.

2.3 Preparation of WK/ZIF-8 sponges

For the preparation of WK/ZIF-8 composite sponges, 0.1 g of WK powders were first added to 1 mL of sodium sulfide nonahydrate solution (10 wt%) and stirred to dissolve. The ZIF-8 powders were then added in different mass ratios (WK: ZIF-8, 10 : 1, 10 : 3, and 10 : 5). Then, 100 μL of SDS solution was added into the WK/ZIF-8 solution and foamed under high-speed rotation (1500 rpm). The solution was lyophilized and exposed to air for 48 h. Finally, after washing with deionized water, WK/ZIF-8 sponges were obtained.

Herein, the sponge modified by ZIF-8 was named WK/Z. In the present study, WK/Z1, WK/Z3, and WK/Z5 were sponges with different mass ratios of WK/ZIF-8 (w/w, 10 : 1, 10 : 3 and 10 : 5), respectively. The sponges without ZIF-8 particles were represented as WK.

2.4 Chemical and physical characterization techniques

2.4.1 FT-IR. The FT-IR spectra of WK, WK/Z1, WK/Z3, and WK/Z5 sponges and ZIF-8 were obtained in the wave number range of 3500–1000 cm^{-1} by employing an FT-IR spectrometer (Magna-560, Nicolet). All samples for FT-IR were characterized by the attenuated total reflectance method.

2.4.2 Microtopography. The morphologies of WK, WK/Z1, WK/Z3, and WK/Z5 sponges and ZIF-8 particles were observed using a field emission scanning electron microscope (SEM, SU8010, HITACHI, Japan). Before observation, all samples were freeze-dried and sputtered with a thin layer of platinum.

2.4.3 Density of sponges. The density of sponges was determined by measuring the weight and dimensions of the samples. The detailed methods can be found in the ESI,† Materials and methods section.

2.4.4 Porosity of sponges. The porosity of sponges was evaluated by a liquid displacement method. The detailed methods can be found in the ESI,† Materials and methods section.

2.4.5 X-ray diffraction (XRD). XRD patterns were recorded under Cu Kα radiation over the 2θ range 5–50° using a Bruker D8-ADVANCE instrument.

2.4.6 Thermogravimetric analyses (TGA). The thermal stability of the prepared sponges was studied using a thermogravimetric analyzer (TGA 4000, PerkinElmer). Thermogravimetric curves were recorded in the range of 35–550 °C at a constant rate of 10 °C min^{-1} under a nitrogen atmosphere.

2.4.7 Water/blood absorption ratio. The water/blood absorption ratios of sponges were determined using the reported method.[27,28] The detailed methods can be found in the ESI,† Materials and methods section.

2.5 Shape memory behavior of sponges

The shape memory properties of sponge samples were evaluated according to the reported method.[3] The detailed methods can be found in the ESI,† Materials and methods section.

The microstructures of sponges in the initial state, fixed state, and recovered state were further observed under a SEM. Sponges with different shapes were compressed into fixed shapes and then soaked in water to investigate shape memory behavior.

2.6 Mechanical properties of the sponges

2.6.1 Compression properties of sponges. The mechanical properties of the sponges were evaluated using an electronic universal testing machine (UTM2102, HITACHI, Japan). The sponges were prepared as cylinders (diameter = 8 mm, height = 8 mm). The sponge was compressed at a strain rate of 10 mm min^{-1} under 60% compression strain (ε). The tests were repeated 3 times for each group.

2.6.2 Rheological test. Rheological experiments were performed using a TA rheometer (DHR-2, USA) equipped with an 8 mm parallel plate at 37 °C. Before the test, 0.2 mol L^{-1} $CaCl_2$ solution was mixed with platelet-rich plasma. Next, the mixed solution was added dropwise to the sponge samples until saturation. Then, the samples were incubated at 37 °C for 30 min. The oscillation frequency was measured from the angular frequency of 0.1 rad s^{-1} to 100 rad s^{-1}. G' was measured to determine the elasticity of the sponge-plasma clots in each group.

2.6.3 Extrusion force test. Briefly, the sponge sample was fixed in a glass tee pipe, and its other end was connected to a pressure meter. A needle was then used to inject water from the last direction of the glass tee pipe until the sponge was extruded and the maximum extrusion force was recorded.

2.7 *In vitro* hemostatic performance

2.7.1 Blood clotting index (BCI). BCI of the sponges was tested according to the previous report.[29] The detailed methods can be found in the ESI,† Materials and methods section.

2.7.2 Blood coagulation time (BCT). BCT was performed using fresh rabbit blood. The detailed methods can be found in the ESI,† Materials and methods section.

2.7.3 Red blood cell (RBC) and platelet adhesion. RBC and platelet adhesion was performed according to a previous report.[30] Before measurement, rabbit whole blood was collected in anticoagulant tubes and centrifuged at 1500 rpm for 10 min to obtain RBC suspension and platelet-rich plasma (PRP). For the RBC adhesion assay, sponge samples (10 mg) were pre-warmed at 37 °C for 30 min, followed by incubation with RBC solution (250 μL) for 30 min at 37 °C. Next, the RBCs that had adhered to the samples were removed by washing the samples five times with PBS. Then, the sample was immersed and rinsed in DI water (5 mL) to lyse adhered RBCs to release hemoglobin. After 1 h, 100 μL of the supernatant was removed and placed into a 96-well microplate, and the absorbance of the solution was measured at 540 nm using a microplate reader (Varioskan LUX, Thermo Fisher Scientific). A solution consisting of 250 μL of erythrocyte suspension and 5 mL of DI water was used as a control group. The percentage of adhered RBCs was calculated using the following equation:

$$\text{RBC adhesion}\,(\%) = \frac{I_s}{I_c} \times 100\% \tag{1}$$

where I_s and I_c are the absorbance values of the sponge samples group and the control group, respectively.

For the platelet adhesion assay, an LDH assay was performed to quantify the degree of platelet adhesion to the different sponges by measuring the LDH released from the lysed platelets. Sponges (10 mg) were pre-warmed in a 24-well plate at 37 °C for 30 min, followed by incubation with PRP (100 μL) at 37 °C for 30 min. Subsequently, non-adherent platelets were removed by gently washing the samples 5 times with PBS (pH = 7.4). To lyse the adhered platelets, the sample was immersed and rinsed in 1% Triton X-100 at 37 °C for 1 h. The number of adherent platelets on the surface of the sponge was determined using an LDH assay kit (Chengdu Yuannuo Tiancheng, China). A solution consisting of 100 μL of PRP, which was not incubated with the sponge, served as the control group. The percentage of adhered platelets was calculated using the following equation:

$$\text{Adhered platelet}\,(\%) = \frac{I_s}{I_c} \times 100\% \tag{2}$$

where I_s and I_c are the absorbance values of the sponges and the control group, respectively.

Additionally, the sponge incubated with PRP and RBC solution was rinsed with PBS and then fixed with 2.5% glutaraldehyde for 4 h. The RBCs and platelets on the sponge were gradually dehydrated with 50%, 75%, 85%, 95%, and 100% ethanol solutions at a time interval of 20 min. Finally, the samples were vacuum-dried and sputter-coated with a layer of platinum. The adhesion of RBCs and platelets (surface and interior) to the vacuum-dried various samples was observed under a SEM.

2.8 Cytocompatibility of sponges

2.8.1 Hemolysis assay. Sponge hemolysis was investigated according to a previous report.[31] Briefly, the sponge (5 mg) was gently mixed with the red blood cell suspension (1 mL). DI water served as the positive control and normal saline as the negative control. After incubation at 37 °C for 4 h, the mixture was centrifuged at 3000 rpm for 10 min, and the supernatant was collected and transferred to a 96-well plate. The absorbance value of the supernatant liquid was measured at 540 nm using a microplate reader (Varioskan LUX, ThermoFisher). The hemolysis ratio of sponges, indicating the percentage of red blood cell disruption, was calculated according to the following equation:

$$\text{Hemolysis }(\%) = \frac{A_\text{s} - A_\text{n}}{A_\text{p} - A_\text{n}} \times 100\% \tag{3}$$

where A_s is the absorbance of the supernatant from the sponge group, A_n is the absorbance of the negative control group, and A_p is the absorbance of the positive control group. All experiments were repeated 3 times (n = 3).

2.8.2 Cell culture. L929 fibroblasts were utilized to investigate the cytocompatibility of the sponges *in vitro*. Cells were cultured in Dulbecco's modified Eagle's medium supplemented with 10% FBS and maintained at 37 °C in a 5% carbon dioxide incubator. The culture medium was refreshed every 2 d.

2.8.3 Cell viability. To study the cell viability, the cytotoxicity of various sponges was evaluated with the Cell Counting Kit 8 (CCK-8) assay using L929 fibroblast cells. Before the test, the sponge samples were irradiated with ultraviolet light for 30 min. Cell suspension solution (100 μL) was inoculated in 96-well plates and cultured for 24 h in an incubator (37 °C, 5% CO_2). Sponges were immersed in a cell culture medium for 24 h to obtain extracts. After incubation, the culture medium was discarded from the wells and replaced with a sponge extract solution (100 μL). Then, the solution was incubated for a further 24 h. Next, 10 μL of the CCK-8 reagent was added to each 96-well plate, and the plates were further incubated for 2 h at 37 °C. The absorbance of each well was measured spectrophotometrically using a microplate reader (Varioskan LUX, Thermo Fisher Scientific) at 450 nm. The resulting absorbance value was proportional to the number of viable cells in the culture. Cells treated without the sponge extract solution were used as a control. The experiment was repeated 3 times. Cell viability was calculated using the following equation:

$$\text{Cell viability }(\%) = \frac{(A_\text{s} - A_\text{b})}{(A_\text{c} - A_\text{b})} \times 100\% \tag{4}$$

where A_s represents the absorbance values of the sponge group, A_c represents the absorbance values of the control group and A_b represents the absorbance of pure CCK8 solution.

The detailed methods of cell live/dead staining tests can be found in the ESI,† Materials and methods section.

2.9 *In vitro* antibacterial activity of the sponges

The antibacterial activity of the sponge was evaluated by using *E. coli* (Gram-negative bacteria) and *S. aureus* (Gram-positive bacteria). The bacterial suspension cocultured with PBS was set as a control group. The bacterial colony counting and live/dead staining were used to characterize the antibacterial ratio and bacterial activity of all the samples. The details of the antibacterial experiment were implemented as in previous reports.[32,33] First, 10 mg of sponges were placed into sterile Eppendorf tubes (2 mL). Then, colonies were diluted to 1 × 10^6 CFU mL^{-1}, added to each tube and incubated at 37 °C for 4 h. The bacterial suspension was then serially diluted 10-fold in PBS. The dilution (100 μL) was spread on a solid nutrient agar plate and incubated at 37 °C for 12 h. Finally, the plates were photographed to count the number of colonies using an automated colony counter. For live/dead cell staining, the bacteria were stained using a live/deadbacklight bacterial viability kit (Invitrogen, USA) and observed using a laser confocal scanning microscope (LCSM, Nikon). All experiments were performed in triplicate, and the bacterial killing ratio was calculated using the following equation:

$$\begin{aligned}&\text{Cell ability of } E.\ coli/S.\ aureus\ (\%)\\&= \frac{\text{colony count of sample}}{\text{colony count of control}} \times 100\%\end{aligned} \tag{5}$$

2.10 Zinc ion release

Inductively coupled plasma mass spectrometry (Agilent, Singapore) was used to determine the release of Zn^{2+} from the WK/Z1, WK/Z3, and WK/Z5 sponges. Briefly, a total of 0.05 g of sponge samples were dipped into 50 mL of ultrapure water and the stirring speed was adjusted to 250 rpm. At time intervals of 10 min, 30 min, 1 h, 3 h, 6 h, 12 h, and 24 h, 10 mL of the supernatant solution was used as the test solution to measure its Zn^{2+} concentration.

2.11 *In vivo* hemostatic performance

All animal experiments were approved by the Experimental Animal Ethics Committee of the Wenzhou Research Institute, University of Chinese Academy of Sciences (Protocol No. WIUCAS21122103). Sprague-Dawley rats (male, weighing 450–500 g) and New Zealand white rabbits (male, weighing 3–4 kg) were purchased from Zhejiang Provincial Laboratory Animal Center. All animal experiments were performed by the same operators to ensure the accuracy of the data and to reduce artificial errors. In animal experiments, the injury without any treatment was set as a blank control. Four animal models were established to obtain the *in vivo* hemostatic efficacy of the sponges, namely, a rat penetrating liver injury model, a rat femoral artery puncture model, a rabbit ear artery hemorrhage model, and a rabbit penetrating liver injury model. At the end of the experiment, the animals were euthanized. The detailed experimental procedures can be found in the ESI,† Materials and methods section.

2.12 Wound healing investigation *in vivo*

SD rats (5–6 weeks old, 200–250 g, male) were randomly divided into four groups: tegaderm film group, commercial gelatin sponge group, WK group, and WK/Z3 sponge group. First, the hair was shaved from the back of the anesthetized rat. Then, a wound (10 mm diameter) was made and infected with 10^7 CFU mL^{-1} *S. aureus* (50 μL) to establish an infected wound model. Sponges were disinfected by ultraviolet and covered the wound surface. Wound healing conditions were recorded by taking photographs on days 0, 5, 10, and 15, and the wound closure area was calculated using the following equation:

$$\text{Wound regeneration }(\%) = \frac{[\text{area}(0\text{ day}) - \text{area}(n\text{ day})]}{\text{area}(0\text{ day})} \times 100\% \tag{6}$$

where area (0 day) and area (n day) refer to the wound areas on days 0 and n, respectively. The wound area was measured using Image J software (V1.8.0.112).

2.13 Histomorphology analysis

For histomorphology analysis, wound tissues from the rats on days 5, 10, and 15 were excised and fixed in 4% paraformaldehyde, and embedded in paraffin. Then, the tissues were sliced. The histological changes were observed under a microscope after staining with hematoxylin and eosin (H&E) stain. Finally, the tissue was immunohistochemically stained with tumor necrosis factor-α (TGF-α) antibodies according to a standard protocol.

2.14 Statistical analysis

The experimental data were expressed as mean ± SD (standard deviation of the mean) and were compared by one-way ANOVA test using SPSS software. *, **, and *** represent P values $<$ 0.05, 0.01, and 0.001, respectively, all of which were considered statistically significant. All quantitative experiments were performed using at least three samples unless otherwise stated.

3. Results and discussion

In this study, we designed and developed a keratin-based antibacterial shape memory hemostatic sponge that could rapidly control massive arterial hemorrhage and non-compressible deep bleeding (Scheme 1a). In the design of the sponge, we took advantage of the thiol groups inherent in keratin, without additional chemical modification on the keratins, which promoted the biocompatibility of the sponge greatly.[27] The Zn^{2+} released by ZIF-8 acted as the cross-linking agent to form Zn–S bonds with sulfhydryl groups, and the cross-linking between sulfhydryl groups led to the formation of S–S bonds. The dynamic exchange reaction between disulfide bonds (S–S) and Zinc–thiolates (Zn–S) led to the formation of a network structure between keratin molecules. By combining keratin and ZIF-8 particles, the effect of ZIF-8 particles on cell viability was reduced, solving the problem of poor mechanical properties and lack of antibacterial effects of the keratin sponge, while the sponge achieved a significant hemostatic effect with the synergistic effect of keratin, ZIF-8, and sponge porosity. (Scheme 1b).

3.1 Fabrication of WK/ZIF-8 sponge

The shape memory WK/ZIF-8 hemostatic sponges are prepared by a simple method as shown in Fig. 1a. Briefly, keratin powders extracted from wool were first dissolved in sodium sulfide nonahydrate solution by stirring and the ZIF-8 nanoparticles prepared by the solvothermal method were then added. The solution was stirred to mix well. After that, the SDS solution was added to the WK/ZIF-8 solution and then foamed at high-speed rotation. Finally, the WK/ZIF-8 sponge was obtained using freeze-drying technology. The synthesized ZIF-8, WK sponges, and WK/ZIF-8 composite sponges were characterized by SEM. As shown in Fig. 1b, ZIF-8 had a uniform rhomboid dodecahedral shape with diameters ranging from

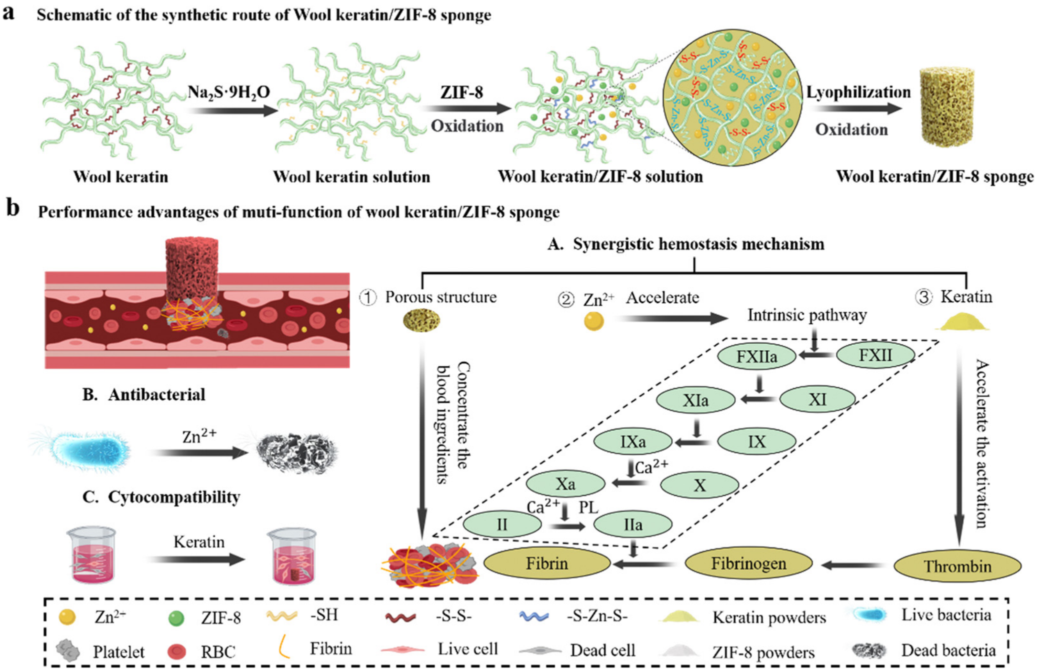

Scheme 1 Design of keratin-based antibacterial shape memory hemostatic sponge and mechanism of hemostasis for rapid control of non-compressible deep bleeding. (a) Schematic of the synthetic route of the WK/ZIF-8 sponge. (b) Performance advantages of multi-functions of the WK/ZIF-8 sponge including incompressible wound hemostasis, antibacterial activity and improved cell vialility.

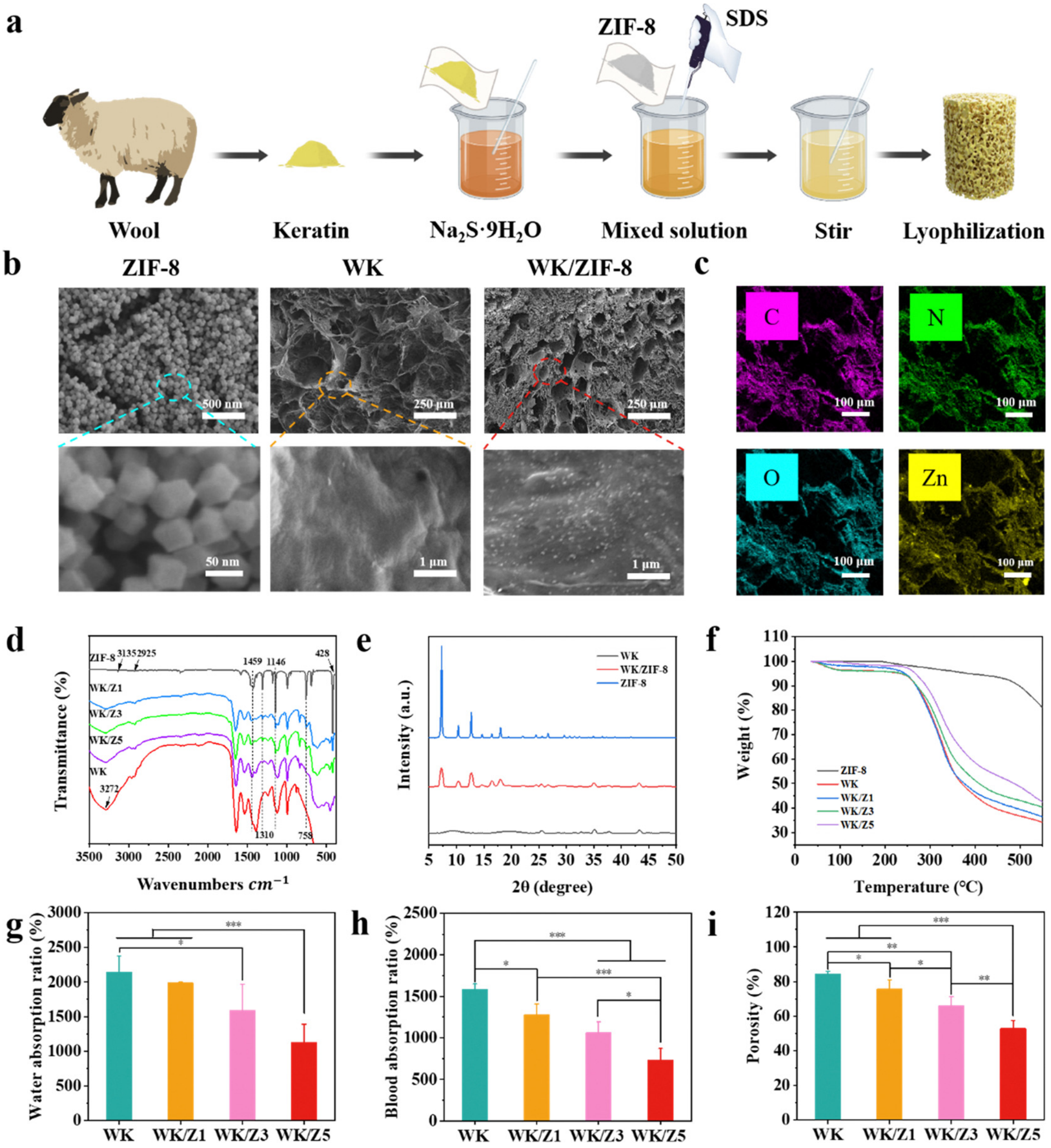

Fig. 1 (a) Schematic illustration of the preparation process. (b) Morphologies of the ZIF-8 particles, WK sponge, and WK/ZIF-8 sponge were observed using SEM and high-resolution SEM. (c) Mapping analysis images for WK/ZIF-8 sponge. (d) FT-IR spectra of ZIF-8, WK, WK/Z1, WK/Z3, and WK/Z5 sponges. (e) XRD patterns of ZIF-8 particles, WK sponge, and WK/ZIF-8 sponge. (f) TGA of ZIF-8, WK, WK/Z1, WK/Z3, and WK/Z5 sponges. (g) Water absorption ratio, (h) Blood absorption ratio, and (i) Porosity of the WK, WK/Z1, WK/Z3, and WK/Z5 sponges. (*$p < 0.05$, **$p < 0.01$, and ***$p < 0.001$).

65 nm to 96 nm evaluated by Image J, which were similar to the previously reported ZIF-8.[17,34] The WK sponge displayed a honeycomb-like and porous structure with appreciable pore interconnectivity. The micrographs of the WK/ZIF-8 composite sponge showed that the addition of ZIF-8 significantly reduced the pore size of the composite sponge. This was because the incorporation of ZIF-8 occupied the keratin network and affected the degree of foaming. At higher magnification, the ZIF-8 particles could be observed in the sponge network and the size was consistent with that of the particles observed by SEM. It was noteworthy that the ZIF-8 particles were not only embedded on the sponge surface but also immobilized inside the sponge. The internal and external distribution of ZIF-8 particles was mainly attributed to the uniform dispersion of ZIF-8 particles in the keratin solution due to vigorous stirring. More importantly, the internal and external distribution of ZIF-8 particles would greatly improve the binding fastness in the composite sponges and play an important role in improving the mechanical properties and antibacterial durability of the sponges.[35] In addition, the EDS spectra of sponges were recorded and the elemental composition of the sponges was identified (Fig. 1c). Unlike the WK sponge (Fig. S1, ESI†), the presence of Zn elements on the WK/ZIF-8 sponge demonstrated the successful incorporation of ZIF-8 particles.

To verify the structure of the sponge, ZIF-8 nano-particles and different sponge groups (Table 1) were analyzed by FT-IR spectroscopy. As shown in Fig. 1d, in the spectra of ZIF-8, the peak at 2925 cm^{-1} was attributed to the N–H stretching vibration of the imidazole moiety present in the ZIF-8 framework and the absorption bands at 428 cm^{-1} correspond to the characteristic Zn–N stretching band present in the ZIF-8 framework.[36] In the spectrum of WK/ZIF-8 sponges, the main differences compared to that of WK sponges are the appearance of peaks at 1457 cm^{-1}, 1310 cm^{-1}, 1146 cm^{-1}, 795 cm^{-1}, and 758 cm^{-1}. The absorption peaks at 1459 cm^{-1}and 1310 cm^{-1} correspond to the whole imidazole ring stretching and the absorption peaks at 1146 cm^{-1} and 758 cm^{-1} are attributed to the =C–H bending and out-of-plane bending, respectively. The absorption peak at 795 cm^{-1} is attributed to the formation of Zn–S bonds[37] (Fig. S2, ESI†). In addition, the characteristic peaks of the protein bands, amide A, amide I, amide II, and amide III bands in the spectra of the sponge samples (Fig. S3 and S4, ESI†), which are identical to the data reported in the literature, indicate that the peptide skeleton of the proteins in the prepared WK/ZIF-8 sponges remained unchanged.[38] It could be seen that the characteristic peaks of the amide A, amide I, amide II, and amide III bands in the sponge gradually decreased with the increase of ZIF-8 content. The reason might be attributed to the reduced percentage of keratin in the same volume of sponge samples measured.

Fig. 1e presented the XRD patterns of the synthesized ZIF-8 particles, WK sponge, and WK/ZIF-8 composite sponge. The positions of the peaks in the XRD pattern of ZIF-8 well matched with those reported in the literature, which further confirmed the structure of the prepared ZIF-8 particles.[39,40] For the WK/ZIF-8 sponge, characteristic peaks were observed at 7.31°, 10.35°, 12.69°, 16.43°, and 18°, corresponding to the (011), (002), (112), (013), and (222) planes of ZIF-8, respectively. The similar crystal characteristic diffraction peaks of WK/ZIF-8 and ZIF-8 in the XRD pattern analysis indicated that WK did not affect the crystal structure of ZIF-8.

The thermal stability of the material was determined by TGA (Fig. 1f), and the WK/ZIF-8 sponges exhibited two loss stages. The first stage was possibly assigned to the evaporation of adsorbed water and the rupture and degradation of peptide bonds in the main chain of the wool keratin molecule. The second stage (starting at around 480 °C) was attributed to the collapse of the ZIF-8 particles. Among the four groups of sponges at 550 °C, the weight loss percentage was the highest for the WK sponge (65.8%), while the WK/Z5 sponge had the lowest weight loss percentage (57.5%). Analysis of the results showed that the addition of ZIF-8 particles improved the thermal stability of the keratin sponge. This was probably because the porous materials such as ZIF-8 had low thermal conductivities, thus improving the thermal properties of the composites.[41]

Table 1 Sample IDs and mass ratios of different sponges

Sample	Mass ratio of wool keratin/ZIF-8 (w/w)
WK	10 : 0
WK/Z1	10 : 1
WK/Z3	10 : 3
WK/Z5	10 : 5

3.2 Water/blood absorption, porosity, and density of the sponge

The ability of hemostatic sponges to rapidly absorb fluid in a short period of time could help them concentrate clotting factors in the blood and promote hemostasis while also helping to rapidly absorb wound exudate to reduce bacterial infections and promote healing.[3,5,6] Therefore, the fluid absorption capacity of different sponges was assessed. As shown in Fig. 1g, h and Fig. S5 (ESI†), the WK sponge had the highest water absorption and blood absorption ratio, and the fastest blood absorption rate of 2141%, 1582%, and 0.18 g cm^{-3} s^{-1}, respectively. The water absorption ratio, blood absorption ratio, and blood absorption rate of the sponges gradually decreased with the increase of ZIF-8 content in the sponges. This was because the density (Fig. S6, ESI†) and dry weight per unit volume of the sponges gradually increased, and the porosity (Fig. 1i) gradually decreased as the incorporation of ZIF-8 in the sponge increased.

3.3 Water triggered shape memory and shape adaptability of the sponge

Hemostatic agents that return to their original shape after contact with blood are called shape-memory hemostatic agents. After being delivered to the bleeding wound sites in a shape-fixed state, shape memory hemostatic sponges could recover their original shape and achieve hemostasis by compressing the bleeding wound.[6] The shape recovery ability was important for stopping deep and narrow non-compressible bleeding.[4] As shown in Fig. 2a, the shape fixed strain (Fig. 2b), recovery strain (Fig. 2c), strain recovery ratio (Fig. 2d), and recovery time (Fig. 2e) of the sponges were quantitatively investigated to determine the shape of the pre-swelled sponge compared to its original free shape.[3]

The results showed that sponges (WK, WK/Z1, WK/Z3, and WK/Z5) were able to achieve a fixed strain of at least 60%. After being immersed in water, the fixed WK and WK/Z1 sponges were able to recover their original shapes within 1 s and 2 s, respectively. The recovery ratios of WK and WK/Z1 sponges were 100%. This rapid water-triggered shape memory process could be clearly observed in Video S1 and Video S2. However, when the content of ZIF-8 was further increased, the shape recovery ratio decreased (97% for WK/Z3) and the recovery time increased (about 6 s for WK/Z3) (Video S3, ESI†). These phenomena could be ascribed to the different pore sizes of the sponges. Compared to the WK sponge, the larger pore size allowed faster water absorption and transport, leading to a higher shape recovery ratio. However, as the ZIF-8 content increased, the pores of the sponges gradually closed. As a result, WK/Z5 exhibited a worsened shape-recovery ratio (Video S4, ESI†). In addition, the hemostatic sponges needed to be shape-adaptable to accommodate various irregular wound shapes. As shown in Fig. 2f, the WK/Z3 sponge was easily tailored into various shapes and its shape recovery properties were not affected after compression and fixation.

The shape memory mechanism of WK/ZIF-8 sponges is schematically represented in Fig. 2g. The excellent water-triggered shape-memory properties of the sponges were mainly attributed to the elastic, stable network structure, and the

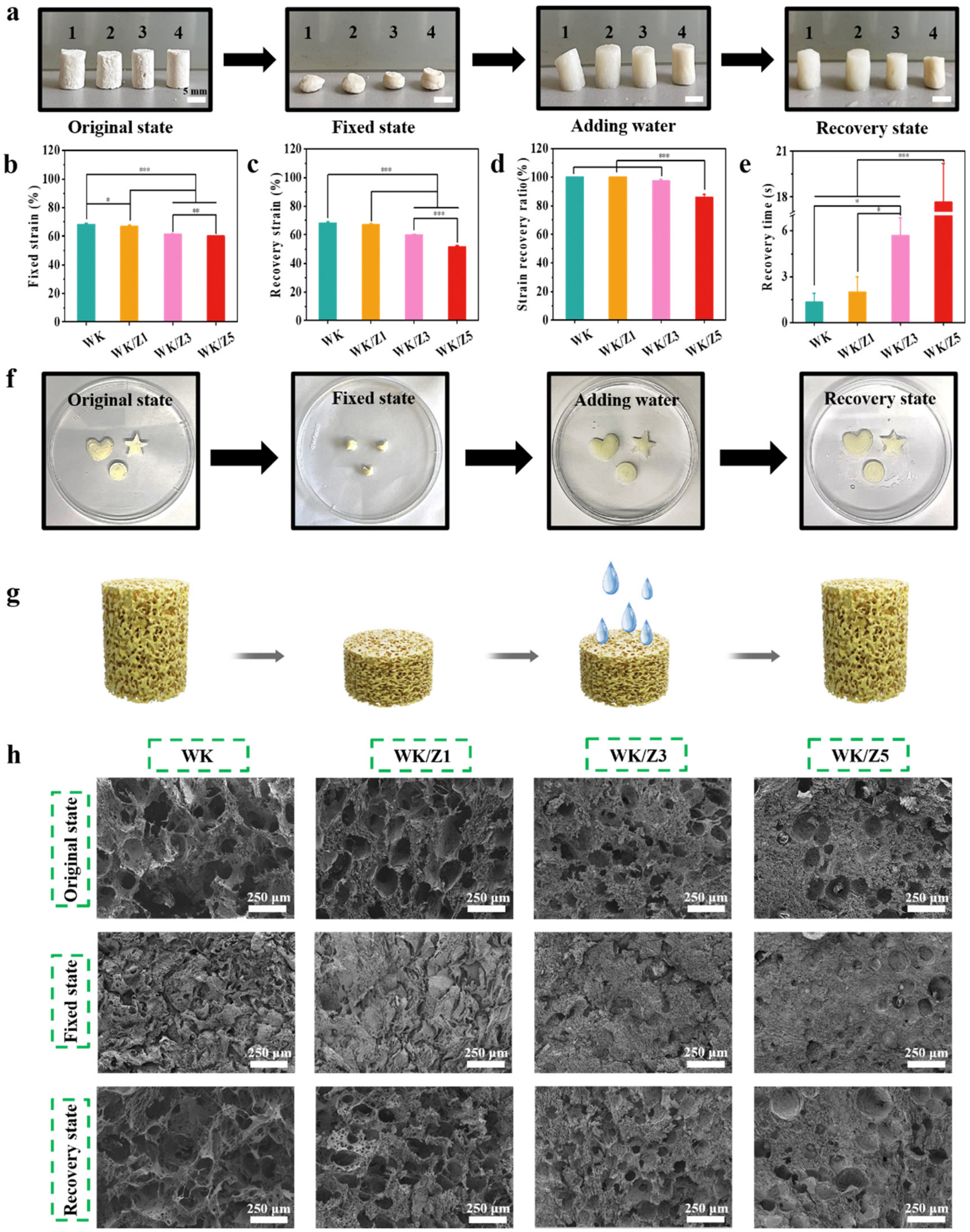

Fig. 2 Water triggered shape memory and shape adaptability of sponges. (a) Photographs of the water-triggered shape recovery of the WK, WK/Z1, WK/Z3, and WK/Z5 sponges. The numbers 1,2,3, and 4 represent WK, WK/Z1, WK/Z3, and WK/Z5 sponges, respectively. (b) Shape fixed strain, (c) shape recovery strain, and (d) strain recovery ratio of different sponges. (e) Shape-recovery time of the compressed sponges. (f) Photographs showing squeeze-dried WK/Z3 sponges with various shapes rapidly returning to their original shapes when immersed in water. (g) Schematic illustration of the water-triggered shape-recovery process of sponges. (h) Microtopography observation of different sponges in original state, fixed state, and recovered state. Scale bar: 250 μm (*$p < 0.05$, **$p < 0.01$, and ***$p < 0.001$).

reversible collapse of their internal pores, which allowed water to freely flow into and out of the pores.[3] When the sponge was compressed, the air was squeezed out of the pores, while the pores of the sponge would collapse, causing the structure to deform. When the external force was removed, the shape of the sponge could remain in a fixed state because the air tension itself was not sufficient to trigger the shape recovery of the sponge.[5] However, if the fixed sponge was in contact with water, the water would be absorbed into the sponge, and the collapsed network structure would rebound, allowing the sponge to regain its original shape. The microtopography recovery of the sponges at their original shapes, fixed shapes, and recovered shapes is shown in Fig. 2h. All of the above results demonstrated that the WK/ZIF-8 sponges possess excellent shape memory ability and shape adaptability, showing their potential for hemostatic applications in irregular, deep, narrow noncompressible wounds.

3.4 Mechanical performance of the sponge

As a hemostatic agent, it should have ideal mechanical strength and flexibility to provide continuous pressure to the bleeding site, which can effectively reduce the blood loss.[4,42] However, sponges prepared using pure natural products generally presented weak mechanical strength, which might hinder their application for hemostasis in various bleeding situations.[3] Therefore, the mechanical strengths of the WK sponge and various WK-based sponges were evaluated by a uniaxial compression test (Fig. 3a). As shown in Fig. 3b, the stress–strain curve showed that the stress of these sponges gradually increased with the increase of ZIF-8 content, indicating that the addition of ZIF-8 particles would help to improve the mechanical strength of the WK sponge. This could be attributed to the addition of ZIF-8 particles reducing the pore structure of the sponge, and the internal and external distribution of ZIF-8 particles improving the network structure of the sponge, which further increased the strength of the sponge.

Additionally, rheological tests were further performed on each group of sponges interacting with platelet rich plasma supplemented with Ca^{2+}. The functional relationship between the storage modulus (G') and angular frequency was investigated under the condition of simulated body temperature (37 °C), and the results are shown in Fig. 3c. The results showed that G' increased significantly with the increase in the incorporated amounts of ZIF-8 particles in sponges. The growth trend of G' might be related to the ZIF-8 particles' increased mechanical strength of the sponges and the effect of Zn^{2+} on thrombosis.[43,44]

Hemostatic materials were subjected to pressure from tissues and fluids when applied to wound sites, so pressure tests were performed to further characterize the mechanical properties of the sponges (Fig. 3d). As shown in Fig. 3e, the maximum pressure gradually increased from the WK to WK/Z5 sponge. Thus, all these results demonstrated that WK/ZIF-8 sponges had good mechanical strength and stability compared to WK sponges, revealing their potential applications as blood-triggered shape recovery hemostatic agents in deep wound hemostasis.

3.5 Hemocompatibility and cytocompatibility of the sponge

As a hemostatic material, hemocompatibility tests were first performed to ensure that hemolysis would not occur when the sponges were used for hemostasis. In this experiment, normal saline and DI water were used as the negative control and the positive control, respectively. After 4 h of incubation with erythrocyte-rich blood, the supernatants obtained by centrifugation of all sponge groups, the negative group, and the positive group are shown in the picture embedded in Fig. 4a. The negative group and the sponge-treated groups were not hemolyzed, while hemolysis occurred in the positive group, and the supernatant was bright red. Results of the hemolysis ratio determined by measuring the OD540 of hemoglobin in the supernatant of each group showed that the hemolysis ratio of sponges was less than 0.3%, which was much less than 5%, which met the international standards for the hemolysis ratio of hemostatic materials (Fig. 4b).[4] Moreover, the pH of the blood solution in which the hemostasis materials were immersed is measured as shown in Fig. 4c. The pH values of all four sponge groups were similar to those of the normal saline group, with almost no significant effect

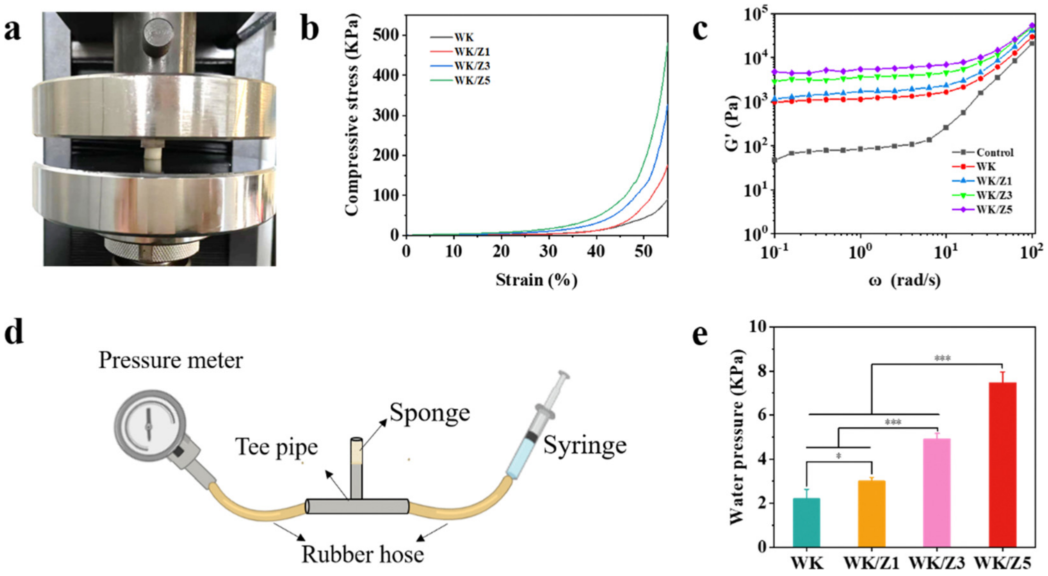

Fig. 3 The mechanical properties of sponges. (a) Image of the sponge during the compression test. (b) The uniaxial compression stress–strain curves of the four sponges. (c) Rheological test results of different sponges after interaction with platelet-rich plasma supplemented with Ca^{2+}. (d) Schematics of the extrusion pressure measurements. (e) Average extrusion pressure of different sponges. (*$p < 0.05$, **$p < 0.01$, and ***$p < 0.001$).

on pH, which would not affect wound healing in an acidic environment. These hemolysis results proved that the sponge had excellent blood compatibility.

Reasonable cytocompatibility is critical for hemostatic agents and wound dressing materials.[6] The cytocompatibility of the material was examined using the CCK-8 assay and live/dead staining assay. The morphology of L929 cells was observed under a LSCM. As shown in Fig. 4d, the viability of L929 cells treated with the WK/Z3 sponge extract at a concentration of 5 mg mL^{-1} was 82.85%, which was slightly lower than that of the control group. As shown in Fig. 4e, a similar conclusion to the CCK-8 assay was drawn from the live/dead staining results, in which the WK/Z3 group showed a large amount of spindle-shaped green fluorescence (live cells) and little red fluorescence (dead cells). Based on the above results, the WK/Z3 sponge had good biocompatibility allowing its application as a potential hemostatic agent or dressing.

3.6 *In vitro* pro-coagulant ability of the sponge

Blood clotting ability is an important characteristic of hemostatic materials.[6] The coagulability of the sponge was evaluated using BCI, BCT, erythrocyte, and platelet adhesion assays. In a dynamic coagulation experiment, the absorbance value of the plasma was measured as the BCI of the sponges (Fig. 5a). The lower the value of BCI, the better the coagulation ability of the sponge. The BCIs of WK, WK/Z1, WK/Z3, and WK/Z5 sponges were 24.07%, 28.58%, 27.49%, and 23.85%, respectively. It was clear that the BCI values of these sponge groups were significantly lower than those of the blank control group (100%) and the gelatin sponge group (50.76%). The commercial gelatin hemostatic sponge was used as a control group. In the blank group, the water used for rinsing turned red due to the presence of large amounts of uncoagulated blood. In contrast, the colors of the blood treated with the sponges were significantly lighter than those of the blank group and the control group (Fig. 5b). The lighter color of the rinsing water indicateed faster coagulation.[45] In the absence of hemostatic sponges, the clotting time of whole blood was 483 s, while the clotting time of commercial gelatin, WK, WK/Z1, WK/Z3, and WK/Z5 sponges was 393 s, 313 s, 309 s, 303 s, and 298 s, indicating that the clotting times of whole blood were significantly shortened after

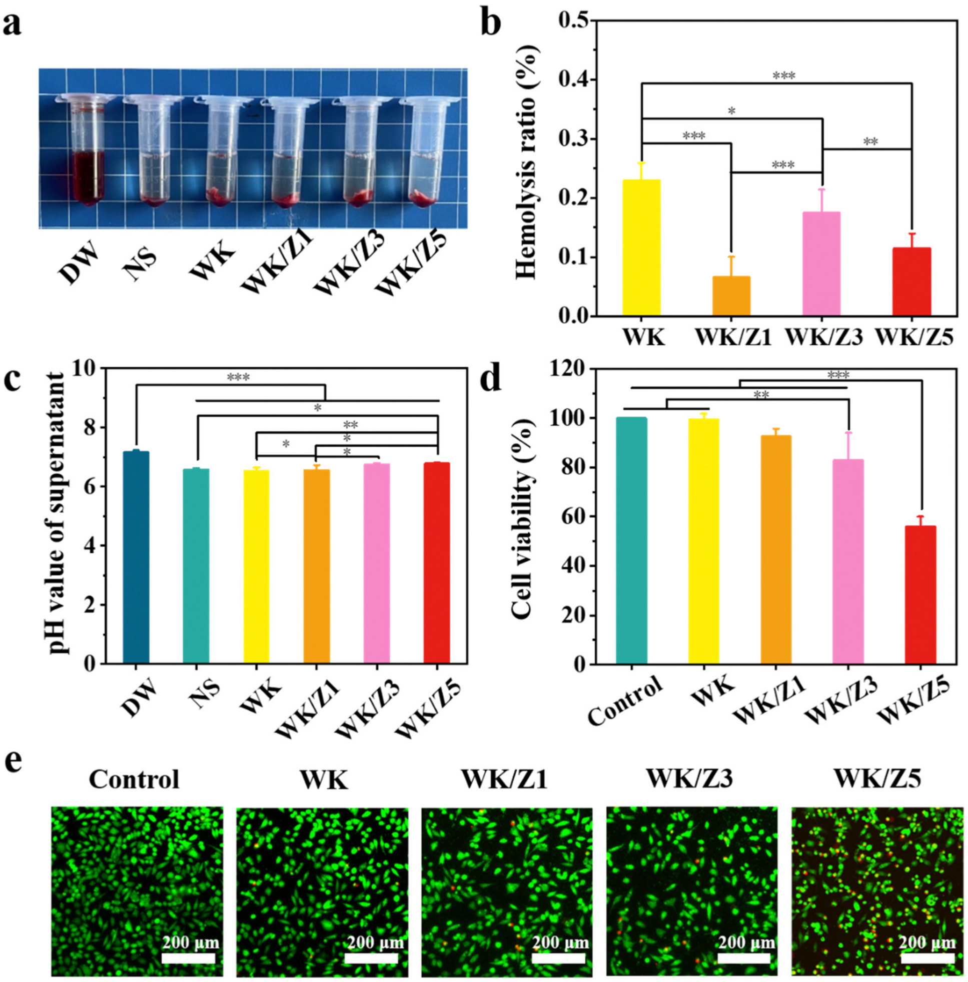

Fig. 4 Hemocompatibility and cytocompatibility evaluation of the sponges. (a) Photographs taken during the hemolysis assay. (b) The hemolysis ratios for different samples. (c) PH value of supernatant in hemolysis test. (d) The cell viability of different groups at 24 h. (e) Live/dead staining of L929 fibroblast cells treated with different groups for 24 h (live cells: green, dead cells: red). (*$p < 0.05$, **$p < 0.01$, and ***$p < 0.001$).

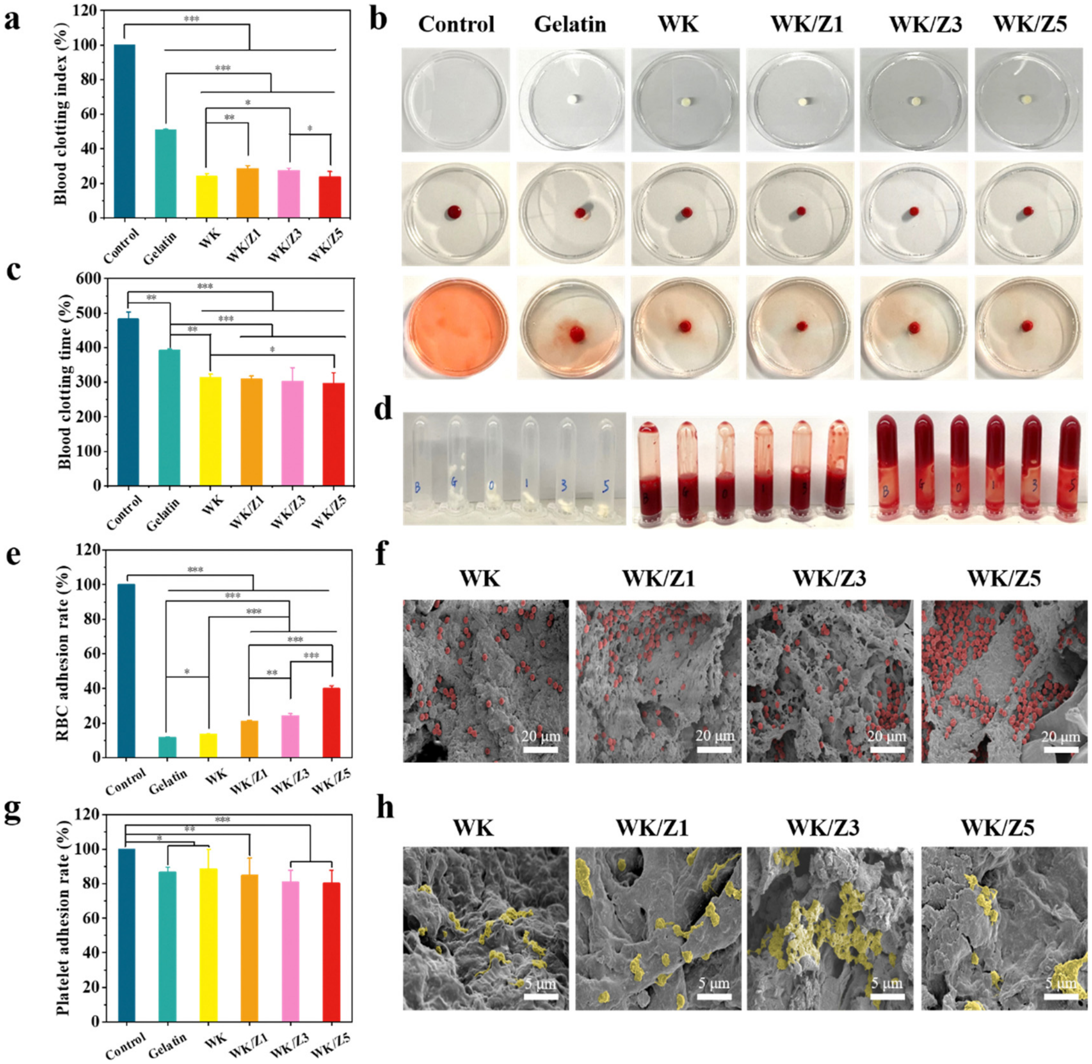

Fig. 5 Hemostatic capacity assessments of different groups *in vitro*. (a) Results of the BCI assay. (b) Photographs on the dynamic whole-blood clotting tests of various samples. (c) BCT of various samples. (d) Photographs of the blood clotting formation process. (e) RBC attachment on various samples. (f) SEM images of RBC attachment on various samples. (g) Platelet adherence on various samples. (h) SEM images of platelet adherence on various samples (*$p < 0.05$, **$p < 0.01$, and ***$p < 0.001$).

contact with the sponges (Fig. 5c and d). It was worth noting that the sponges with ZIF-8 particles showed a superior hemostatic effect, and the hemostatic effect was enhanced with the increase of ZIF-8 content, indicating that ZIF-8 particles further promoted blood coagulation based on keratin sponge hemostatic properties.

The hemostatic mechanism of the sponge was further investigated by RBC and platelet adhesion assays. As shown in Fig. 5e, the sponge in the experimental group had a higher erythrocyte adhesion ratio compared to the commercial gelatin sponge. It was found that the erythrocyte adhesion ratio on the sponge increased with the content of ZIF-8 nanoparticles. This was because the positively charged Zn^{2+} could bind to the negatively charged cell membrane, thereby promoting the erythrocyte aggregation.[46]

As shown in Fig. 5g, the results of the LDH assay showed that the adhesion rates to platelets were above 80% for all sponge groups. Furthermore, the interaction of erythrocytes/platelets with sponges after blood absorption was investigated by SEM. As shown in Fig. 5f, erythrocytes adhered to the sponge surfaces to form aggregates. The number of erythrocytes on the surface of the WK/ZIF-8 sponges was much higher than that on the gelatin sponge. It could be clearly seen that the pseudopodia of the platelets were clearly visible on the surface of the sponge, indicating that the platelets had been successfully activated and participated in hemostasis (Fig. 5h). The above phenomenon suggested that the WK/ZIF-8 sponges could enhance the coagulation effect by enriching the red blood cells and activating platelets in the plasma.

3.7 The antibacterial ability of the sponge

To protect the wound tissue from external bacterial infection, an ideal hemostatic agent should have excellent antibacterial properties.[47,48] The antibacterial properties of all sponges were evaluated using *S. aureus* and *E. coli in vitro*. Fig. 6a showed representative images of the bacterial culture plate. After co-culturing bacteria with each group of sponges, we found that the number of colonies increased for the WK sponge, compared to the control group, suggesting that the WK sponge promoted the proliferation of bacteria, as materials without antibacterial activity could aggravate the infection.[49,50] However, when ZIF-8 nanoparticles containing Zn^{2+} were added to the sponges, compared to the control group, the number of colonies was slightly reduced for the WK/Z1 sponge, and the number of colonies on the plates was significantly reduced for the WK/Z3 sponge and the WK/Z5 sponge, indicating that with the increase of ZIF-8, the antibacterial ability of the sponge increased. Further quantitative analysis of the antibacterial activity of the sponge showed that the viabilities of *E. coli* and *S. aureus* co-cultured with the WK/Z3 sponge were 48.94% and 7.22%, respectively (Fig. 6b and c). The reason might be attributed to the fact that *E. coli* had a double-layered membrane compared to the thick but porous cell membrane of *S. aureus*, for which the dense outer membrane provided additional protection.[51] Additionally, the live/dead bacterial viability assays revealed that the WK/Z1, WK/Z3, and WK/Z5 sponge images contained red fluorescence attributed to dead bacteria, whereas the WK sponge group images showed live

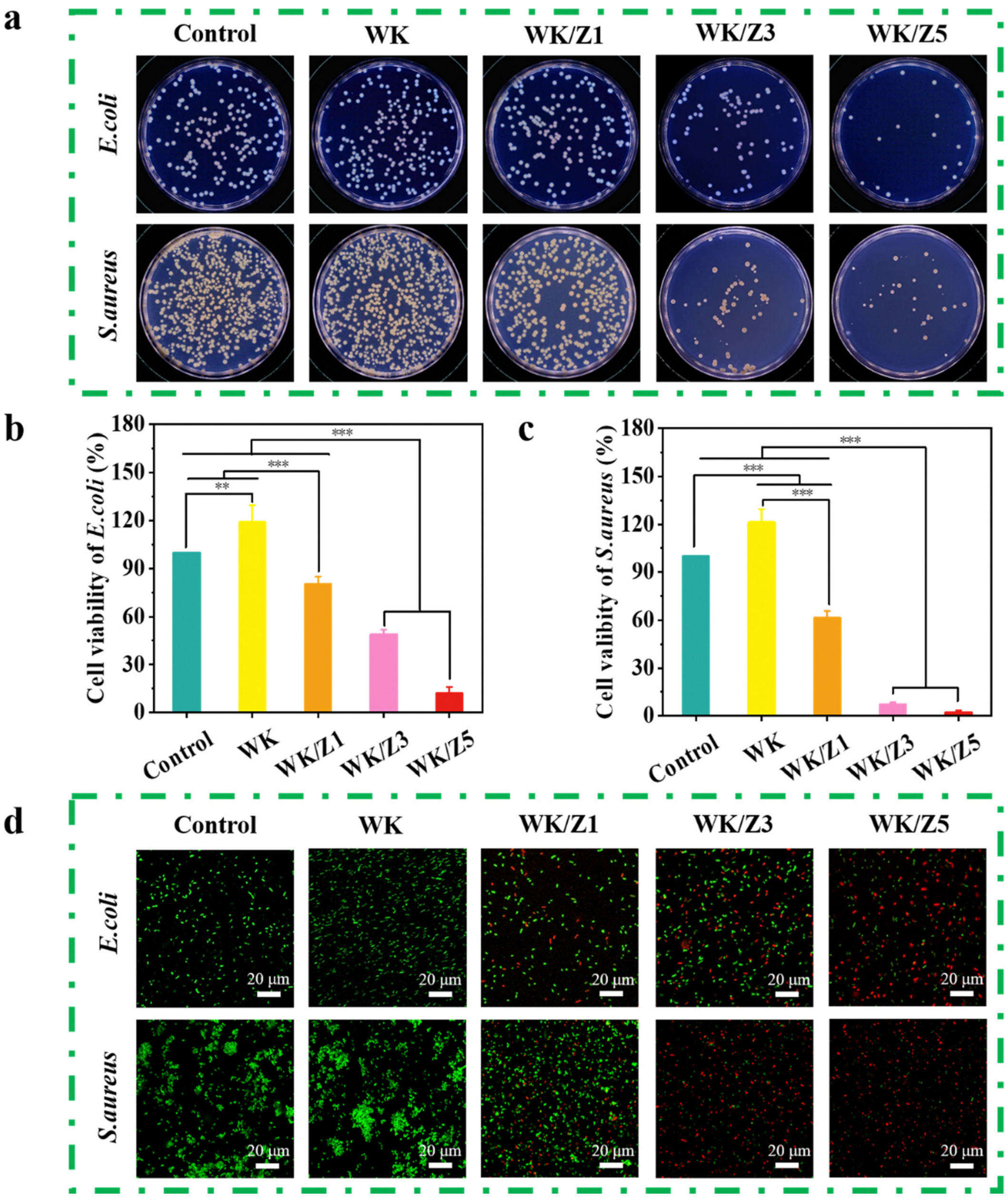

Fig. 6 Antibacterial evaluation of all samples. (a) Representative display picture of the bacterial culture plate. Quantitative antibacterial test results of different sponges to (b) Gram-negative *E. coli* and (c) Gram-positive *S. aureus*. (d) Representative live/dead images of *E. coli* and *S. aureus* after contact with sponges. (*$p < 0.05$, **$p < 0.01$, and ***$p < 0.001$).

bacteria with strong green fluorescence, indicating that the sponge had no bactericidal ability (Fig. 6d).

The antibacterial activity of the WK/Z3 sponge was due to the synergy of the following factors: (i) the release of Zn^{2+} from the ZIF-8 particles could adsorb bacteria on their surfaces by electrostatic interaction and disturb the charge balance, further killing the bacteria by penetrating the cell wall to destroy its protein and DNA;[17,20,52] (ii) the swelling of the sponge in the bacterial solution facilitated the release and contact of Zn^{2+} with the bacteria; (iii) the antibacterial ZIF-8 particles were immobilized inside and on the surface of the sponge, which ensured the durability of the antibacterial performance.[35]

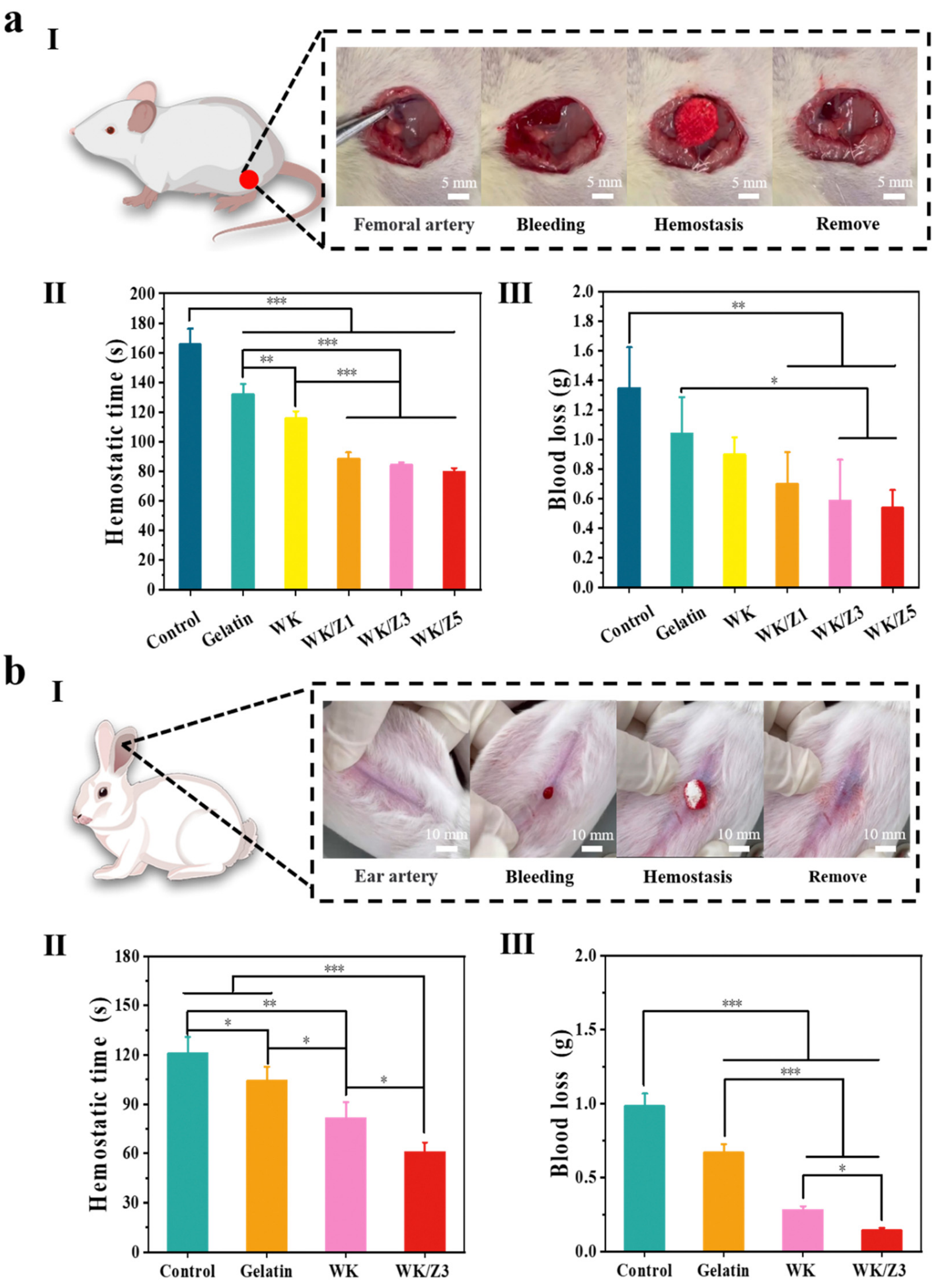

Fig. 7 *In vivo* hemostatic capacity evaluation of sponges. (a) rat femoral artery puncture model. (b) rabbit ear artery hemorrhage model. (I) Schematic diagram of the animal models and hemostatic process pictures of WK/Z3 sponge (II) quantitative statistics of hemostasis time and (III) blood loss for different groups (*$p < 0.05$, **$p < 0.01$, and ***$p < 0.001$).

Afterwards, the release behavior of Zn^{2+} was investigated. The curves of Zn^{2+} release from the WK/Z1 sponge, WK/Z3 sponge, and WK/Z5 sponge in the ultrapure water are shown in Fig. S7 (ESI†). During the first ten minutes, the Zn^{2+} concentration were released by the WK/Z3 sponge was 0.4023 mg L^{-1}. This showed that sponges were able to release Zn^{2+} in time during hemostasis and promote hemostasis. Moreover, the gradual increase in the concentration of zinc ions released by the WK/Z3 sponge over 24 hours suggested a stable and sustained release of Zn^{2+}, which was favorable for sustained antibacterial and long-lasting effective effects on wound healing.

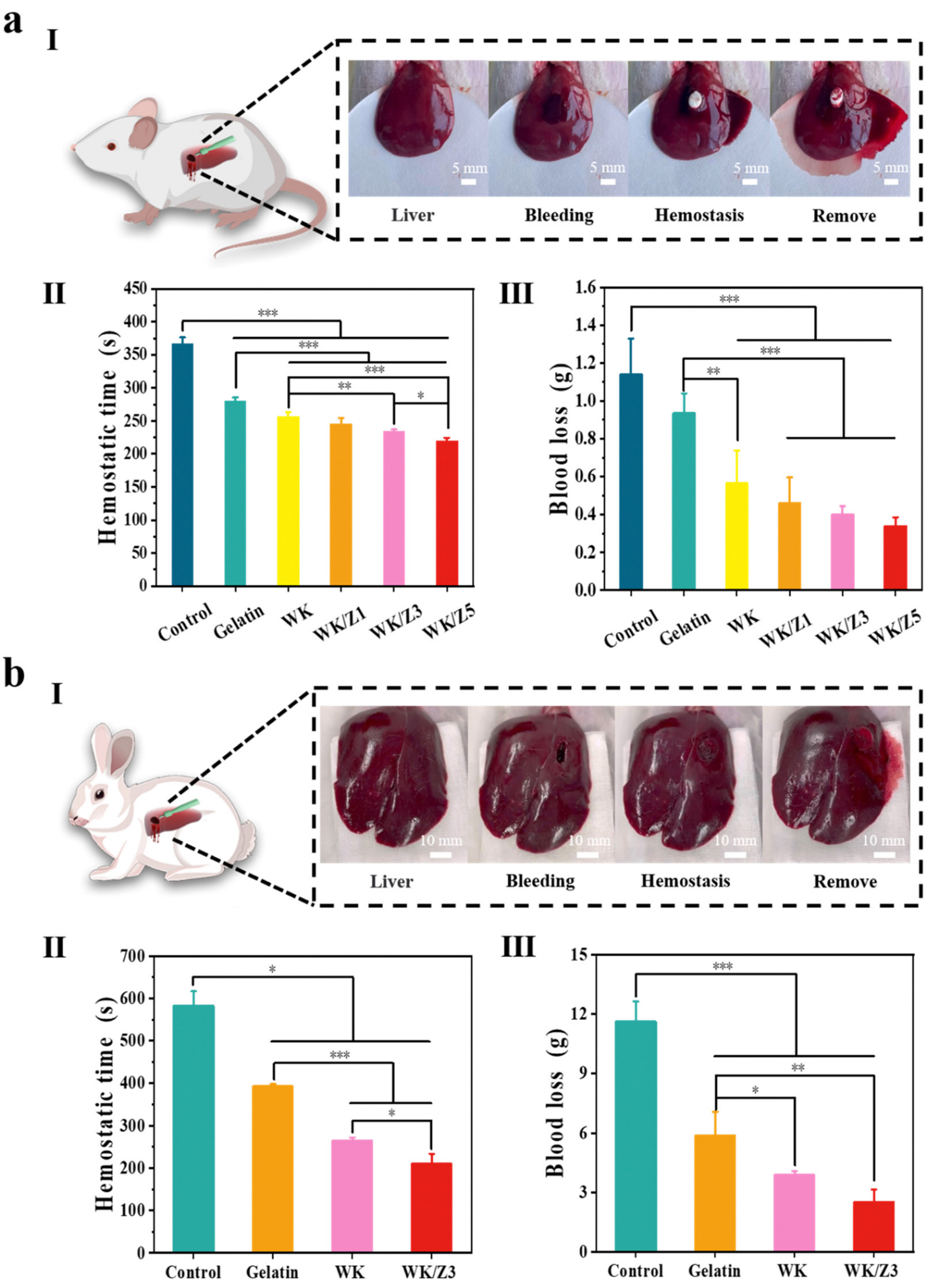

Fig. 8 *In vivo* hemostatic capacity evaluation of sponges. (a) Rat penetrating liver injury model. (b) Rabbit penetrating liver injury model. (I) Schematic diagram of the animal models and hemostatic process pictures of WK/Z3 sponge, (II) quantitative statistics of hemostasis time and (III) blood loss for different groups (*$p < 0.05$, **$p < 0.01$, and ***$p < 0.001$).

Taken together, the above *in vitro* results indicated that the WK/Z3 sponge could not only promote hemostasis and wound healing but also prevent wound infection after hemostasis.

3.8 *In vivo* hemostatic properties of the sponges

As a novel antimicrobial hemostatic agent, the WK/Z3 sponge achieved a good balance between mechanical properties, antibacterial properties, biocompatibility, and procoagulant capacity, which was verified by various experiments. Therefore, the WK/Z3 sponge was selected for further investigation *in vivo*.

To simulate a massive bleeding wound, a rat femoral artery puncture model (Fig. 7a$_{\mathrm{I}}$) and a rabbit ear artery hemorrhage model (Fig. 7b$_{\mathrm{I}}$) were used to assess the hemostatic capacity of various samples. In the rat femoral artery puncture model, the hemostasis time (Fig. 7a$_{\mathrm{II}}$) and blood loss (Fig. 7a$_{\mathrm{III}}$) of the WK/Z3 sponge group were lower than those of the blank control, gelatin sponge group, WK sponge, and WK/Z1 sponge groups. In the rabbit ear artery hemorrhage model, it was obvious that the WK/Z3 sponge exhibited the shortest clotting time (Fig. 7b$_{\mathrm{II}}$) and the least amount of bleeding (Fig. 7b$_{\mathrm{III}}$).

To simulate a narrow and deep non-compressible bleeding wound, where traditional hemostatic materials were generally less effective, we prepared a rat liver penetrating injury model (Fig. 8a$_{\mathrm{I}}$) and a rabbit liver penetrating injury model (Fig. 8b$_{\mathrm{I}}$). In the rat liver penetrating injury model, the hemostasis time of the blank group was 366.33 s. After treatment with a commercial gelatin sponge, WK, WK/Z1, WK/Z3, and WK/Z5 sponges, the hemostasis times were 280.67 s, 256.67 s, 245.67 s 234.33 s, and 220 s, respectively (Fig. 8a$_{\mathrm{II}}$). The blood loss exhibited the same trend as the hemostasis time. The blood loss of the blank group

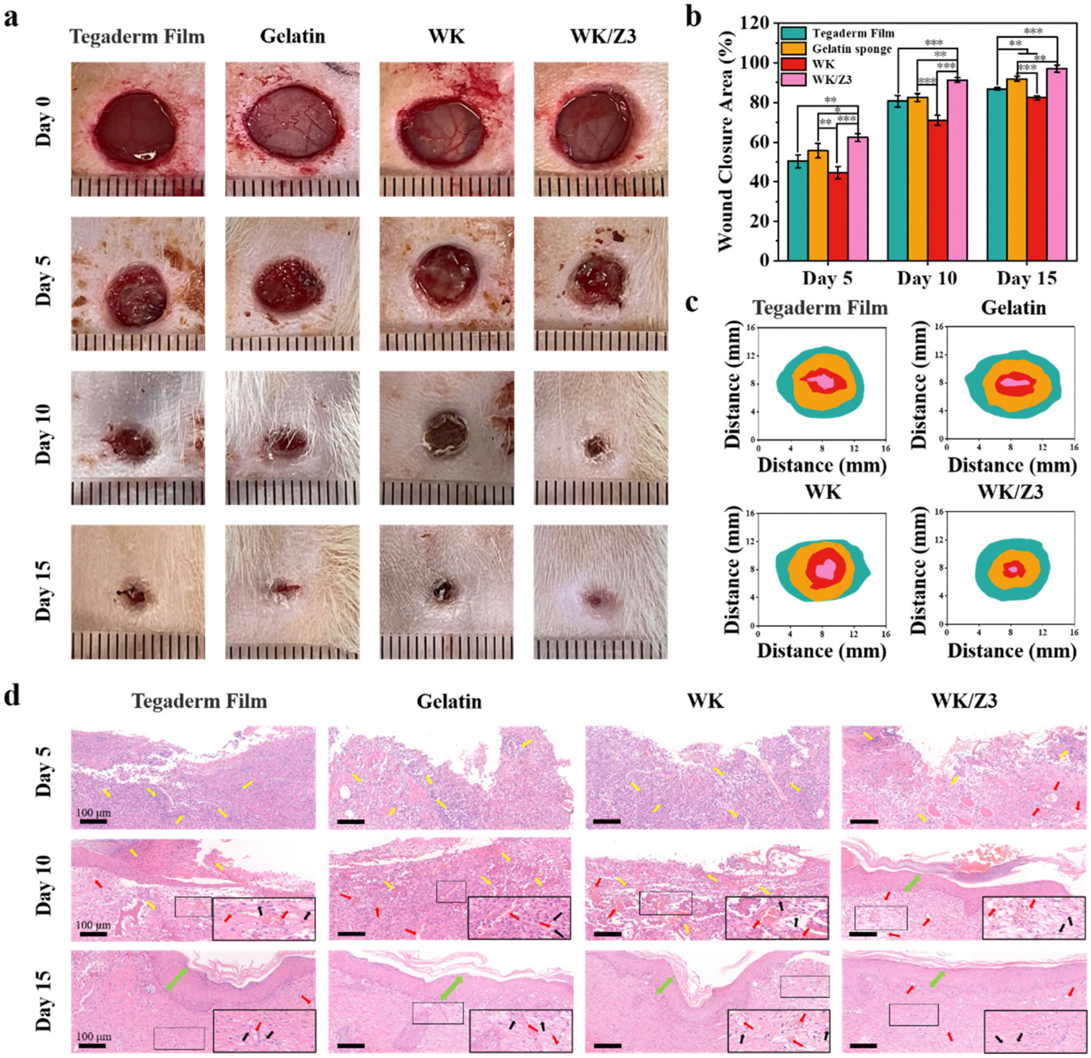

Fig. 9 SD rats full-thickness skin defect wound healing assessment for different samples. (a) Representational photographs of skin wound infection with *S. aureus* and treatment with Tegaderm Film, gelatin sponge, WK sponge, and WK/Z3 sponge. (The diameter of the circle is 10 mm.) (b) Wound closure rate and (c) The corresponding traces after treatment with Tegaderm Film, gelatin sponge, WK sponge, and WK/Z3 sponge at 0, 5, 10 and 15 days. (d) H&E staining evaluation of wound healing for Tegaderm Film, gelatin sponge, WK sponge, and WK/Z3 sponge after 5, 10, and 15 days. (Yellow arrows: inflammatory cells, red arrows: blood vessels, black arrows: fibroblasts, green arrows: the border of the epidermal layer.) ($^{*}p < 0.05$, $^{**}p < 0.01$, and $^{***}p < 0.001$).

was 1.14 g, and the blood losses of the commercial gelatin sponge group, WK, WK/Z1, WK/Z3, and WK/Z5 sponges group were 0.93 g, 0.56 g, 0.46 g, 0.40 g, and 0.34 g, respectively (Fig. $8a_{III}$). The results showed that the WK/Z3 sponge could significantly shorten the coagulation time and reduce blood loss compared to the blank control group and commercial gelatin sponge. In the rabbit penetrating liver injury model, the hemostasis time of the blank control and gelatin sponge was 582 s and 393 s, respectively. Hemostasis was achieved after 265 s and 210 s in the WK and WK/Z3 groups, respectively (Fig. $8b_{II}$). Meanwhile, the blood loss results showed that the blood losses in the experimental sponge groups were lower than those in the blank control and gelatin sponge groups (Fig. $8b_{III}$). Furthermore, the difference in blood loss and hemostasis time between the WK/Z3 sponge group and the WK sponge group indicated that the ZIF-8 nanoparticles had a facilitating effect on hemostasis.

The above experimental results showed that WK/Z3 sponge efficiently controlled lethal arterial bleeding and non-compressible hemorrhage and exhibited better hemostatic efficiency than commercial gelatin sponge. The excellent hemostatic effect of WK/Z3 could be attributed to the following reasons: on the one hand, the WK/Z3 sponge with good mechanical properties could be customized into different shapes, then compressed and fixed to be inserted into narrow, deep, and irregular wounds conveniently. Because of its porous structure and excellent fluid absorption ability, the sponge inserted into the wound could absorb plasma, and concentrate blood to entrap aggregated hemocytes, while rapidly expanding to fill the wound and exert pressure on the wound wall, thereby playing a good physical blocking and hemostatic effect. On the other hand, keratin could accelerate the activation of thrombin and subsequently activate fibrinogen, leading to the formation of insoluble fibrinogen polymers.[15,53] In addition, Zn^{2+} released from ZIF-8 particles could enhance platelet aggregation and serve as a cofactor to induce activation of coagulation factor XII to instigate the rest of the intrinsic coagulation cascade, leading to the generation of thrombin and fibrin.[24,25] The synergistic effect of the above reasons explained the good hemostatic effect of the WK/Z3 sponge, indicating that the WK/Z3 sponge had great potential for use in lethal non-compressive hemorrhage application.

3.9 *In vivo* wound healing performance of the sponge

The infected full-thickness wound healing model was established by introducing *S. aureus* to the wound sites to investigate the wound healing ability of the WK/Z3 sponge *in vivo*. Fig. 9a showed the images and schematic graphs of the wounds at days 0, 5, 10, and 15 for each of the different treatment conditions. During the wound healing process, the WK/Z3 sponge group achieved faster wound healing at each test time point and showed the highest wound healing effect compared to the control group, the commercial gelatin sponge group, and the WK sponge group (Fig. 9b). The images of the wounds and the corresponding quantitative size of the wound area at different time points were presented in Fig. 9c. These results indicated that the WK/Z3 sponge could stimulate *S. aureus*-infected wound healing due to its good antibacterial properties.

During wound healing, low levels of inflammation promote wound healing, but severe inflammatory cell infiltration damages the wound tissue.[6] The histological status of the wound samples and inflammation during the healing periods were analyzed using H&E staining and immunohistochemical staining. TNF-α was selected for the expression of inflammation. As shown in Fig. 9(d) and Fig. S8, S9 (ESI†), the blank control group, the commercial gelatin sponge group, and the WK sponge group showed severe inflammatory cell infiltration, indicating that the healing process was still in the inflammatory phase. In contrast, wounds in the WK/Z3 group contained few inflammatory cells on day 5; this might be attributed to the antibacterial properties of WK/Z3 to kill the bacteria near wounds, reducing the inflammation responses. After 10 days of treatment, the inflammatory cells decreased and blood vessels formed in the blank control group, the commercial gelatin sponge group, and the WK sponge group. At this time point, the inflammatory cells disappeared from the WK/Z3 sponge-treated wounds, and a thin epidermis formed. Moreover, by post-operative day 15, the epidermis over the WK/Z3 sponge-treated wound had matured and the new skin had returned to normal. However, the blank control group, the commercial gelatin sponge group, and the WK sponge group showed incomplete epithelium. Based on these results, it can be inferred that the WK/Z3 sponge had great potential in wound treatment.

The superior performance of the WK/Z3 sponge in infected wound healing is mainly due to its multifunctional properties. First, WK/Z3 sponges were able to stop bleeding quickly due to their excellent hemostatic properties, which played a key role in the early stages of the healing process. Second, the WK/Z3 sponge after absorbing exudate could continuously maintain a moist and anti-infective environment during the repair process, which was essential for the infected wound healing.[54,55] In addition, the keratin could provide a scaffolding function to the injured tissue, allowing rapid cell infiltration and granulation or reparative response.[56]

4. Conclusion

Keratin sponges are promising candidates for use as emergency hemostats. However, pure keratin materials generally have low mechanical strength and lack the necessary stability for hemostatic applications. Additionally, keratin does not possess antibacterial properties, which are needed to cope with the harsh environment of patients with uncontrolled bleeding prior to hospitalization or surgery. To overcome these issues, a series of WK/ZIF-8 composite sponges were prepared with various ratios (ZIF-8/WK: 0%, 10%, 30%, and 50%). The structure of the final product was characterized using Fourier-transform infrared spectroscopy, X-ray diffraction, scanning electron microscopy, and thermogravimetric analysis. The WK/Z3 sponge achieved a good balance between mechanical properties, antibacterial properties, biocompatibility, and procoagulant capacity, which was verified by various experiments. Further tests, including rat femoral artery puncture, rat liver penetrating injury, rabbit ear artery hemorrhage, and rabbit liver penetrating injury, confirmed that the WK/Z3 sponge could accelerate hemostasis and reduce blood loss compared to the WK sponge and commercial gelatin sponge groups. Moreover, the WK/Z3 sponge could promote wound healing in full-thickness skin defects infected with *S. aureus* without causing a significant inflammatory response. In summary, our study provides a highly promising approach for improving the performance of keratin-based sponges, and shape memory sponges can quickly control bleeding and prevent bacterial infection, demonstrating their great potential for clinical applications as multifunctional hemostatic agents.

Conflicts of interest

There are no conflicts to declare.

Acknowledgements

This project was supported by Wenzhou Science and Technology Major Project (Grant No. ZY2019018, ZY2022028), Wenzhou Institute, University of Chinese Academy of Sciences startup fund (Grant No. WIUCASQD2019006), the Zhejiang Province Welfare Technology Applied Research Project (Grant No. LGF20C100002), the Wenzhou Science and Technology Public Project (Grant No. Y20210264), and the Key Laboratory of diagnosis and treatment of severe hepato-pancreatic diseases of Zhejiang Province (Grant No. 2018E10008).

References

1 G. Castellini, S. Gianola, A. Biffi, G. Porcu, A. Fabbri, M. P. Ruggieri, C. Coniglio, A. Napoletano, D. Coclite, D. D'Angelo, A. J. Fauci, L. Iacorossi, R. Latina, K. Salomone, S. Gupta, P. Iannone and O. Chiara, *World J. Emerg. Surg.*, 2021, **16**, 41.
2 J. J. Morrison and T. E. Rasmussen, *Crit. Care Clin.*, 2017, **33**, 37–54.
3 X. Zhao, B. Guo, H. Wu, Y. Liang and P. X. Ma, *Nat. Commun.*, 2018, **9**, 2784.
4 S. Lv, M. Cai, F. Leng and X. Jiang, *Carbohydr. Polym.*, 2022, **288**, 119369.
5 L. Zheng, Q. Wang, Y. S. Zhang, H. Zhang, Y. Tang, Y. Zhang, W. Zhang and X. Zhang, *Chem. Eng. J.*, 2021, **416**, 129136.
6 Y. Zhang, Y. Wang, L. Chen, J. Zheng, X. Fan, X. Xu, G. Zhou, N. Ullah and X. Feng, *Biomaterials*, 2022, **285**, 121546.
7 M. I. Bajestani, S. Kader, M. Monavarian, S. M. Mousavi, E. Jabbari and A. Jafari, *Int. J. Biol. Macromol.*, 2020, **142**, 790–802.
8 K. Zuniga, A. Isaac, S. Christy, N. Wrice, L. Mangum, S. Natesan, L. Burnett, R. Christy and C. Kowalczewski, *Int. J. Mol. Sci.*, 2022, **23**, 4100.
9 Y. Esparza, N. Bandara, A. Ullah and J. Wu, *Mater. Sci. Eng., C*, 2018, **90**, 446–453.
10 S. Sadeghi, J. Nourmohammadi, A. Ghaee and N. Soleimani, *Int. J. Biol. Macromol.*, 2020, **147**, 1239–1247.
11 W. Li, F. Gao, J. Kan, J. Deng, B. Wang and S. Hao, *Colloids Surf., B*, 2019, **175**, 436–444.
12 M. B. Rahmany, R. R. Hantgan and M. Van Dyke, *Biomaterials*, 2013, **34**, 2492–2500.
13 S. Feroz, N. Muhammad, J. Ranayake and G. Dias, *Bioact. Mater.*, 2020, **5**, 496–509.
14 Z. K. Moay, L. T. H. Nguyen, P. Hartrianti, D. P. Lunny, D. Leavesley, Y. O. Kok, S. J. Chong, A. W. C. Chua, S.-I. Tee and K. W. Ng, *Int. J. Mol. Sci.*, 2021, **22**, 8594.
15 Z. Sun, X. Chen, X. Ma, X. Cui, Z. Yi and X. Li, *J. Mater. Chem. B*, 2018, **6**, 6133–6141.
16 C. D. Tran and T. M. Mututuvari, *Langmuir*, 2015, **31**, 1516–1526.
17 Y. Cai, J. Guan, W. Wang, L. Wang, J. Su and L. Fang, *J. Food Sci.*, 2021, **86**, 3550–3562.
18 J. Chen, X. Zhang, C. Huang, H. Cai, S. Hu, Q. Wan, X. Pei and J. Wang, *J. Biomed. Mater. Res., Part A*, 2017, **105**, 834–846.
19 W. Teng, Z. Zhang, Y. Wang, Y. Ye, E. Yinwang, A. Liu, X. Zhou, J. Xu, C. Zhou, H. Sun, F. Wang, L. Zhang, C. Cheng, P. Lin, Y. Wu, Z. Gou, X. Yu and Z. Ye, *Small*, 2021, **17**, e2102315.
20 T. A. Makhetha, S. C. Ray and R. M. Moutloali, *ACS Omega*, 2020, **5**, 9626–9640.
21 X. Meng, J. Guan, S. Lai, L. Fang and J. Su, *RSC Adv.*, 2022, **12**, 10005–10013.
22 Y. Xiao, M. Xu, N. Lv, C. Cheng, P. Huang, J. Li, Y. Hu and M. Sun, *Acta Biomater.*, 2021, **122**, 291–305.
23 V. Ravinayagam and S. Rehman, *Saudi. J. Biol. Sci.*, 2020, **27**, 1726–1736.
24 M. Pan, Z. Tang, J. Tu, Z. Wang, Q. Chen, R. Xiao and H. Liu, *Mater. Sci. Eng., C*, 2018, **85**, 27–36.
25 T. T. Vu, J. C. Fredenburgh and J. I. Weitz, *Thromb. Haemost.*, 2013, **109**, 421–430.
26 C. Cui, T. Wu, F. Gao, C. Fan, Z. Xu, H. Wang, B. Liu and W. Liu, *Adv. Funct. Mater.*, 2018, **28**, 1804925.
27 M. Chen, X. Ren, L. Dong, X. Li and H. Cheng, *Int. J. Biol. Macromol.*, 2021, **182**, 1259–1267.
28 J. Liu, M. Qu, C. Wang, Y. Xue, H. Huang, Q. Chen, W. Sun, X. Zhou, G. Xu and X. Jiang, *Small*, 2022, **18**, e2106172.
29 X. Yang, M. Chen, P. Li, Z. Ji, M. Wang, Y. Feng and C. Shi, *J. Mater. Chem. B*, 2021, **9**, 1568–1582.
30 X. Yang, W. Liu, Y. Shi, G. Xi, M. Wang, B. Liang, Y. Feng, X. Ren and C. Shi, *Acta Biomater.*, 2019, **99**, 220–235.
31 X. Yang, W. Liu, G. Xi, M. Wang, B. Liang, Y. Shi, Y. Feng, X. Ren and C. Shi, *Carbohydr. Polym.*, 2019, **222**, 115012.
32 B. Chen, H. Zhang, J. Qiu, S. Wang, L. Ouyang, Y. Qiao and X. Liu, *Small*, 2022, **18**, e2201766.
33 X. Yang, C. Wang, Y. Liu, H. Niu, W. Zhao, J. Wang and K. Dai, *ACS Appl. Mater. Interfaces*, 2021, **13**, 36709–36721.
34 X. Zheng, Y. Zhang, L. Zou, Y. Wang, X. Zhou, L. Yao, Z. Wang, C. Li and Y. Qiu, *Colloids Surf., B*, 2020, **193**, 111127.
35 X. Zheng, Y. Zhang, Z. Wang, Y. Wang, L. Zou, X. Zhou, S. Hong, L. Yao and C. Li, *Nanotechnology*, 2020, **31**, 375707.

36 A. R. Chowdhuri, B. Das, A. Kumar, S. Tripathy, S. Roy and S. K. Sahu, *Nanotechnology*, 2017, **28**, 095102.

37 M. Zahiri, M. Shafiee Afarani and A. M. Arabi, *J. Fluoresc.*, 2019, **5**, 1227–1239.

38 L. Olariu, B. G. Dumitriu, C. Gaidau, M. Stanca, L. M. Tanase, M. D. Ene, I. R. Stanculescu and C. Tablet, *Polymers*, 2022, **14**, 1125.

39 I. Kohsari, Z. Shariatinia and S. M. Pourmortazavi, *Int. J. Biol. Macromol.*, 2016, **91**, 778–788.

40 H. Chen, J. Yang, L. Sun, H. Zhang, Y. Guo, J. Qu, W. Jiang, W. Chen, J. Ji, Y. W. Yang and B. Wang, *Small*, 2019, **15**, e1903880.

41 L. Qian, D. Lei, X. Duan, S. Zhang, W. Song, C. Hou and R. Tang, *Carbohydr. Polym.*, 2018, **192**, 44–51.

42 T. L. Landsman, T. Touchet, S. M. Hasan, C. Smith, B. Russell, J. Rivera, D. J. Maitland and E. Cosgriff-Hernandez, *Acta Biomater.*, 2017, **47**, 91–99.

43 S. A. Chaudhry, M. Serrata, L. Tomczak, S. Higgins, J. Ryu, D. Laprise, K. Enjyoji, R. Bekendam, V. Kaushik, R. Flaumenhaft and P. K. Bendapudi, *J. Thromb. Haemost.*, 2020, **18**, 2318–2328.

44 H. Yang, X. Lan and Y. Xiong, *Gels*, 2022, **8**, 279.

45 K. Zhang, X. Bai, Z. Yuan, X. Cao, X. Jiao, Y. Li, Y. Qin, Y. Wen and X. Zhang, *Biomaterials*, 2019, **204**, 70–79.

46 Y. Liang, M. Li, Y. Huang and B. Guo, *Small*, 2021, **17**, e2101356.

47 M. Li, Z. Zhang, Y. Liang, J. He and B. Guo, *ACS Appl. Mater. Interfaces*, 2020, **12**, 35856–35872.

48 H. Yuan, L. Chen and F. F. Hong, *ACS Appl. Mater. Interfaces*, 2020, **12**, 3382–3392.

49 S. Amin Yavari, S. M. Castenmiller, J. A. G. van Strijp and M. Croes, *Adv. Mater.*, 2020, **32**, e2002962.

50 Z. Li, B. Li, X. Li, Z. Lin, L. Chen, H. Chen, Y. Jin, T. Zhang, H. Xia, Y. Lu and Y. Zhang, *Carbohydr. Polym.*, 2021, **267**, 118155.

51 S. Duan, X. Zhao, Z. Su, C. Wang and Y. Lin, *ACS Appl. Bio Mater.*, 2020, **3**, 3673–3680.

52 A. Abednejad, A. Ghaee, J. Nourmohammadi and A. A. Mehrizi, *Carbohydr. Polym.*, 2019, **222**, 115033.

53 J. Wang, S. Hao, T. Luo, Q. Yang and B. Wang, *Mater. Sci. Eng., C*, 2016, **68**, 768–773.

54 C. Wang, M. Wang, T. Xu, X. Zhang, C. Lin, W. Gao, H. Xu, B. Lei and C. Mao, *Theranostics*, 2019, **9**, 65–76.

55 X. Li, H. Bai, Y. Yang, J. Yoon, S. Wang and X. Zhang, *Adv. Mater.*, 2019, **31**, e1805092.

56 T. Aboushwareb, D. Eberli, C. Ward, C. Broda, J. Holcomb, A. Atala and M. Van Dyke, *J. Biomed. Mater. Res., Part B*, 2008, **90**, 45–54.